



Journal of Geophysical Research: Solid Earth

RESEARCH ARTICLE

10.1002/2017JB015057

Special Section:

Rock Physics of the Upper Crust

Key Points:

- Experimental measurements of mechanical fracture closure and fluid flow in rough fractures are presented
- A method to predict fully hydro-mechanically coupled effects in rough fractures is demonstrated
- Mechanical fracture closure behavior and corresponding fluid pressure response are captured by numerical simulations

Correspondence to:

D. Vogler, davogler@ethz.ch

Citation:

Vogler, D., Settgast, R. R., Annavarapu, C., Madonna, C., Bayer, P., & Amann, F. (2018). Experiments and simulations of fully hydro-mechanically coupled response of rough fractures exposed to high-pressure fluid injection. *Journal of Geophysical Research: Solid Earth*, *123*, 1186–1200. https://doi.org/10.1002/2017JB015057

Received 3 OCT 2017 Accepted 9 JAN 2018 Accepted article online 11 JAN 2018 Published online 7 FEB 2018

Experiments and Simulations of Fully Hydro-Mechanically Coupled Response of Rough Fractures Exposed to High-Pressure Fluid Injection

D. Vogler^{1,2}, R. R. Settgast³, C. Annavarapu³, C. Madonna⁴, P. Bayer⁵, and F. Amann^{4,6}

¹ Geothermal Energy and Geofluids, Institute of Geophysics, ETH Zurich, Zurich, Switzerland, ²Transport Processes and Reactions Laboratory, Institute of Process Engineering, ETH Zurich, Zurich, Switzerland, ³ Atmospheric, Earth, and Energy Division, Lawrence Livermore National Laboratory, Livermore, CA, USA, ⁴Department of Earth Sciences, ETH Zurich, Zurich, Switzerland, ⁵Institute of new Energy Systems, Ingolstadt University of Applied Sciences (THI), Ingolstadt, Germany, ⁶Chair of Engineering Geology, RWTH Aachen, Aachen, Germany

Abstract In this work, we present the application of a fully coupled hydro-mechanical method to investigate the effect of fracture heterogeneity on fluid flow through fractures at the laboratory scale. Experimental and numerical studies of fracture closure behavior in the presence of heterogeneous mechanical and hydraulic properties are presented. We compare the results of two sets of laboratory experiments on granodiorite specimens against numerical simulations in order to investigate the mechanical fracture closure and the hydro-mechanical effects, respectively. The model captures fracture closure behavior and predicts a nonlinear increase in fluid injection pressure with loading. Results from this study indicate that the heterogeneous aperture distributions measured for experiment specimens can be used as model input for a local cubic law model in a heterogeneous fracture to capture fracture closure behavior and corresponding fluid pressure response.

1. Introduction

Hydro-mechanically (HM) coupled fluid flow is an actively researched topic in reservoir engineering, enhanced geothermal systems (EGSs) and CO_2 sequestration (Figueiredo, Tsang, Rutqvist, Bensabat, & Niemi, 2015; Figueiredo, Tsang, Rutqvist, & Niemi, 2015; Gu et al., 2014; Guo et al., 2016; Rutqvist & Stephansson, 2003). Specifically, hydro-mechanically coupled processes in EGS often have critical effects on the efficiency of heat extraction from the reservoir (Fu et al., 2016; Guo et al., 2016). Induced seismic hazards associated with EGS and CO_2 sequestration can also be mitigated through a greater understanding of hydro-mechanical processes that take place in the subsurface (McClure & Horne, 2014a, 2014b).

Hydro-mechanically coupled processes span several length scales (e.g., laboratory to field scale). Here the fracture aperture and asperity length scales at smaller scales often significantly affect the fluid flow pathways through the fractures at the macroscopic scale. Several studies have therefore focused on studying this effect at the laboratory scale (e.g., Esaki et al., 1999; Raven & Gale, 1985; Renshaw, 1995; Watanabe et al., 2008, 2009; Zimmerman & Bodvarsson, 1996; Zimmerman et al., 1991). The mechanical and hydraulic effects in fractures are commonly represented with the mechanical and hydraulic aperture ($a_{\rm mech}$ and $a_{\rm hyd}$), respectively. Here the mechanical aperture signifies the distance between the two fracture surfaces. The hydraulic aperture relates flow rate and pressure gradient across a fracture to an averaged aperture which can be computed under the assumption that the fracture consists of two parallel plates (cubic law) (e.g., Louis, 1969; Witherspoon et al., 1980). Laboratory investigations on fluid flow in fractures, both with and without mechanical deformation, have concluded that averages of the mechanical and hydraulic aperture across the fracture can normally not be equated (e. q., Brown, 1987; Chen et al., 2000; Cook, 1992; Esaki et al., 1999; Hakami & Larsson, 1996; Lee & Cho, 2002; Oron & Berkowitz, 1998; Renshaw, 1995; Raven & Gale, 1985; Vogler, Amann, et al., 2016; Zimmerman & Bodvarsson, 1996; Zou et al., 2015). While the specific relationship between hydraulic and mechanical aperture is not fully understood, a number of studies found the hydraulic aperture to be generally smaller than the mechanical aperture, both with and without mechanical loading of the fracture (Esaki et al., 1999; Hakami & Larsson, 1996; Raven & Gale, 1985; Vogler, Amann, et al., 2016).

©2018. American Geophysical Union. All Rights Reserved.

To further understanding of the relationship between mechanical and hydraulic aperture (Esaki et al., 1999; Rutqvist & Stephansson, 2003; Xiong et al., 2011; Zou et al., 2015), a number of research efforts have been dedicated to determining the specific relation between a_{mech} and a_{hvd} (e. g., Cook, 1992; Park et al., 2013; Wang et al., 2015; Zimmerman et al., 1991; Zimmerman & Bodvarsson, 1996). Specifically, a reduction of the mechanical aperture has been linked to an increase in tortuosity, which in turn weakens assumptions made in the cubic law (e.g., Brown, 1987; Tsang, 1984). The impact of fracture normal strength and topography on the hydro-mechanical behavior in a fracture has therefore been thoroughly scrutinized (e. g., Li et al., 2008; Park et al., 2013; Pyrak-Nolte & Morris, 2000; Walsh, 2003; Yeo et al., 1998), and a number of empirical relationships relating effective normal stress and fracture normal stiffness (e. g., Barton et al., 1985; Gu et al., 2014) have been proposed.

It is understood that the mechanical aperture, contact stresses, and the fluid flow field and pressures associated with the hydraulic aperture can exhibit a tightly coupled relationship. A number of studies have investigated permeability enhancement due to pressure injection on the reservoir scale, where asperity-scale processes such as the influence of contact stresses and regions on stress and flow distribution in the fracture are averaged with a Barton and Bandis relationship or poroelastic deformation (Barton et al., 1985; Figueiredo, Tsang, Rutgvist, Bensabat, & Niemi, 2015; Figueiredo, Tsang, Rutgvist, & Niemi, 2015; Gu et al., 2014). However, to our knowledge, a numerical study that computes the tightly coupled behavior between mechanical deformation and fluid flow on the asperity scale for heterogeneous fractures, as well as the corresponding stress field in the rock mass, does not yet exist. On the laboratory scale, most previous simulation approaches for processes in rough fractures focus either on fluid flow or the mechanical behavior of the fracture and do not incorporate full hydro-mechanical coupling (e. g., Nemoto et al., 2009; Tsang, 1984; Watanabe et al., 2008, 2009; Wang et al., 2015). On the field scale, fractures are commonly approximated as parallel plates (Derode et al., 2013; Min et al., 2013), and mechanical and hydraulic properties are averaged over large regions (Cappa & Rutqvist, 2011; Derode et al., 2013; Figueiredo, Tsanq, Rutqvist, Bensabat, & Niemi, 2015; Figueiredo, Tsanq, Rutqvist, & Niemi, 2015). Predictive simulations need to be able to compute effective mechanical and hydraulic properties and behavior from geometric information of the fracture and bulk rock properties, which are either well known or can be measured in simple experiments.

We address these issues through a fully coupled hydro-mechanical model with a provision for heterogeneous mechanical and hydraulic properties in fractures. Our objective is to capture the effect of fracture roughness at the asperity scales on the macroscopic stress perturbations in the rock mass, flow channeling in the fractures, and fluid pressure response to mechanical deformation. We compare our numerical model with experiments investigating (1) bulk mechanical behavior of the fracture and (2) hydro-mechanical effects during loading. The proposed method is implemented in GEOS: a flexible multiscale, multiphysics simulation environment developed at Lawrence Livermore National Laboratory (Settgast et al., 2017).

2. Methods

2.1. Experimental Setup

Granodiorite specimens from the Grimsel Test Site, Switzerland, were used for this set of experiments, with uniformly distributed mineral grains with a size of 3 to 8 mm. Three specimens of cylindrical shape with a diameter of 122 mm and a height of 243, 225, and 206 mm (Specimens A, B, and C) were prepared (Figures 1b and 1c). Saw cut notches were cut in the specimens at the targeted height of the fracture and subsequently loaded with two prisms from the top and bottom. This generated artificial fractures in the middle of the specimens, with a fracture plane approximately normal to the cylinder axis (Figure 1). A 2,000 kN servocontrolled uniaxial press (Walter and Bai AG, Switzerland) was used to apply axial loading to the specimens. For all experiment sets, preloads of 0.14 MPa were applied to the specimens. Two sets of experiments were performed:

- 1. Bulk mechanical behavior of the fracture. First, the dry fracture was incrementally loaded from 0.25 to 10 MPa, after which the load was subsequently decreased again to 0.25 MPa. Step sizes were 0.25 MPa for loads between 0.25 and 1 MPa, while step size between 1 and 10 MPa was 1 MPa.
- 2. Hydro-mechanical effects during loading. A centric hole of 8 mm diameter was drilled into the top half of the specimen along the specimen axis. Metal tubing with an outer diameter of 8 mm and an inner diameter of 4 mm was placed in the hole to prevent leakage of fluid into the specimen before the fluid reached the fracture. Fluid injection was controlled with a syringe pump (Teledyne Isco, Model 260D). The ISCO pump used to inject fluid into the rock specimen has an associated error of 0.5% of the set point at the full range (up to 51.7 MPa), which results in a maximum error of 0.25 MPa. The pump was used to inject a constant

21699356, 2018. 2, Downloaded from https://agupubs.onlinelibrary.wiley.com/doi/10.1002/2017JB015057, Wiley Online Library on [27/11/2025]. See the Terms and Conditions (https://onlinelibrary.wiley.

and-conditions) on Wiley Online Library for rules of use; OA articles are governed by the applicable Creative Commons License

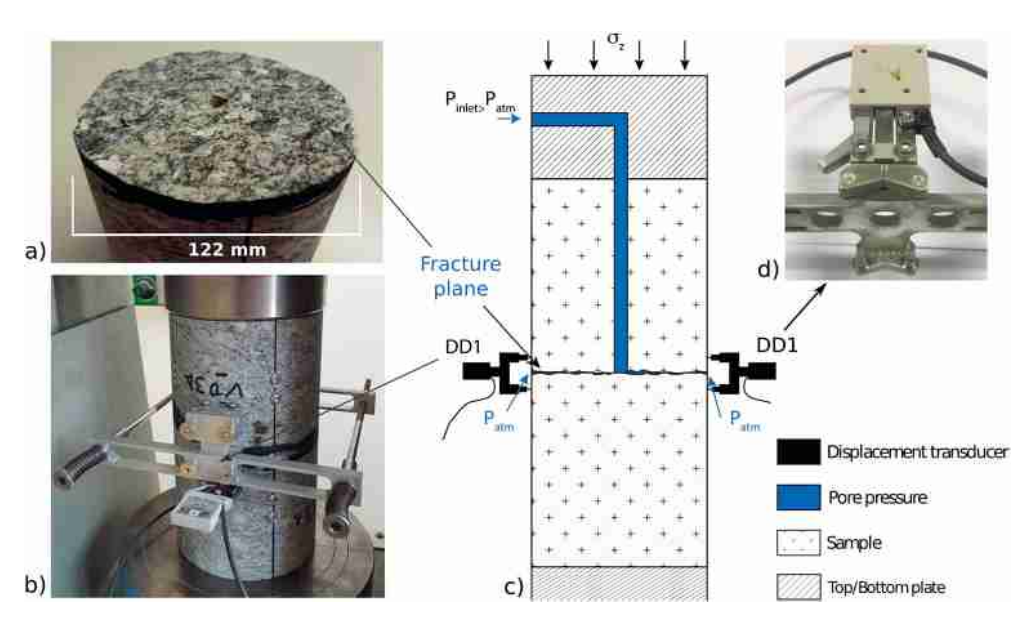


Figure 1. Experimental setup with cylindrical specimen. The fracture is situated half-way up the cylinder, with the fracture plane normal to the cylinder axis. (c) A schematic of experiment Set II, with supplementary figures depicting (a) a tested fracture plane, (b) the testing configuration with displacement transducers, and (d) the displacement transducers. The displacement transducer measures if top and bottom part of the sensor are displaced relative to each other.

flow rate of 5 mL/min into the fracture for all specimens. Axial loads were stepwise increased from 0.25 to 1 MPa (i.e., in steps of 0.25 MPa) and subsequently from 1 to 10 MPa (i.e., in steps of 1.0 MPa) during fluid injection, and changes in injection pressure in response to axial load changes were recorded. Figure 1 shows the experimental setup with the pump, which was used to inject fluid into the fracture and measure the injection pressure, the axial stress σ_{7} which was applied to the top of the specimen, the borehole from the center of the top of the specimen to the center of the fracture, the displacement transducers, and the outflow of the fracture at the fracture boundary to atmospheric fluid pressure conditions.

A displacement transducer (type DD1, HBM, Germany) was employed in both experiment sets to measure specimen deformation during loading. Specimen deformation is measured with four contact points to the specimen, with two contact points approximately 5 cm apart along the specimen axis on each side the specimen (positioned diagonally across the specimen, see Figure 1c). The maximum error associated with the DD1 sensor measurement is ±0.05% of the measured displacement. The error associated with the applied normal loads has a maximum value of 1 kN for the maximum normal load applied in the presented experiments (120 kN).

Compression tests on intact rock samples from the same core material used to create the experiment specimens yielded elastic Young's modulus between 10 and 12 GPa. This property allowed calculation of deformation from the measurements of the displacement of the fractured core. Specifically, fracture closure was calculated from the sensor data by subtracting the theoretical intact rock mass deformation from the displacement transducer.

Before and after the experimental procedure, high-resolution photogrammetric scans of the surface were recorded with an ATOS Core 3D scanner (GOM mbH, Germany) (GOM mbH, 2017). The ATOS core 3D scanner projects fringe patterns on the object surface, which are recorded by two cameras. A phase shift based on sinusoidal intensity distribution results in a pattern, which enables calculation of the three-dimensional (3-D) surfaces. The photogrammetry scanner was calibrated with length deviation errors between 0.009 and 0.027 mm. The optimized calibration deviations were 0.014 \pm 0.001 Pixel. Specifically, this means that standardized objects (e.g., the diameter of a perfectly round sphere) can be measured with maximum deviations between 9 and 27 μ m. To avoid problems with different reflectivities of minerals, the fracture surfaces were coated with a white spray. The applied spray can add a few micrometers to the height of the fracture surface.

After scanning, the fracture surfaces are represented as three-dimensional point clouds and have a spatial density which is roughly between 30 and 60 unique vertices per square millimeter. The fractures are further prepared by removing any extraneous details of the specimen scan, which is not part of the fracture surface. Afterward, the fracture plane is reoriented such that the normal vector to the fracture surface is oriented along the z axis. The x-y plane is defined as the plane that provides the least squares fit of the given fracture surface. Reorientation is obtained by aligning the eigenvectors of the fracture surface plane with the primary coordinate system. This fit is only performed for the lower fracture surface, whereas the upper fracture surface is fitted to the lower fracture surface. Fitting of the fracture surfaces is achieved with the commercial optimization tool GOM Inspect (GOM mbH, Germany), which offers best fit alignment of objects (e.g., two fracture surfaces) consisting of large number of degrees of freedom. The top fracture surface is aligned to the bottom fracture surface such that contact between the two fracture surfaces is established in three points, while the integral over the aperture field is minimized.

Once fracture top and bottom are aligned, the surfaces were mapped onto a regular grid in the x-y plane with 100 µm spacing between grid points in both directions. The aperture field can then be computed by subtracting the z values of the lower fracture surface from the upper fracture surface. The resolution in the z direction is set to the precise distance (aperture) computed between the two gridded surfaces. Similar approaches to derive fracture surfaces and corresponding aperture fields were also employed by Vogler et al. (Vogler, 2016; Vogler, Amann, et al., 2016; Vogler, Walsh, Bayer, & Amann, 2017; Vogler, Walsh, Dombrovski, & Perras, 2017).

Between experiment Sets I and II, 30 loading cycles were performed on the specimens. This ensures that no plastic deformation should be expected for experiment Set II. No gouge material production or fracture surface damage was observed for experiment Set II. This yields one set of aperture fields for experiment Set I and another set of aperture fields for experiment Set II.

2.2. Numerical Simulations

The numerical simulations presented in this work are performed using the GEOS simulation framework. GEOS is a massively parallel multiphysics simulation framework developed at Lawrence Livermore National Laboratory, which offers coupling of the presented method with other capabilities of GEOS, including simulation of hydraulic fracture stimulation in two and three dimensions (Fu et al., 2015; Settgast et al., 2012, 2014, 2017; Vogler, Settgast, et al., 2017); modeling geochemical transport and reaction (Walsh et al., 2012, 2013) geothermic drawdown (Fu et al., 2016); fracture shearing (Annavarapu et al., 2015), matrix flow, and heat transport (Guo et al., 2016); and simulations of immiscible fluid flow (Walsh & Carroll, 2013). Preliminary results of the current study, using the GEOS framework, can also be found in Vogler, Settgast, et al. (2016) and Vogler (2016).

The fully coupled HM solver in GEOS utilizes a finite element method to model solid body deformation and a finite volume method to model the fluid flow in fractures and the matrix. For this study, matrix flow is neglected due to the low permeability of Grimsel granodiorite and the relatively short time scales involved. Fluid flow in the fracture applies lubrication theory (i.e., parallel plate assumptions) on volumes between fractured element faces (Settgast et al., 2017):

$$\frac{\partial}{\partial t}(\rho_w a) - \frac{1}{12\mu} \nabla \cdot \rho_w a^3 \nabla(p + \rho g z) = 0, \tag{1}$$

where μ is the dynamic viscosity, p is the fluid pressure, a is the fracture aperture, and ρ_w is the fluid density. The aperture a is computed as $a = \mathbf{u} \cdot \mathbf{n}$ with the displacement across the fracture surface \mathbf{u} and the face normal vector \mathbf{n} . Solid deformation of the body Ω with external boundaries Γ is discretized using a standard Galerkin finite element method on the equations of static equilibrium. Integration over the elements in the solid domain gives the solid body residual as

$$(R_{\text{solid}}^{e})_{hi} = \int_{\Gamma_{t}^{e}} \Phi_{h} t_{i} dA + \int_{\Gamma^{e}} \Phi_{h} (f_{i}^{c} + c_{i} - pn_{i}) dA$$

$$- \int_{\Omega^{e}} \Phi_{h,j} T_{ij} dV + \int_{\Omega^{e}} \Phi_{h} \rho_{m} b_{i} dV,$$
(2)

with nodal index h, spatial direction i, finite element shape function Φ , solid body density ρ_m , the Cauchy stress tensor T_{ii} , body force (gravity) b_{ii} and externally applied traction t_{i} . The penalty method is used to enforce

frictional contact conditions under small-deformation assumptions (Annavarapu et al., 2015). The residual for the rate of fluid mass in a finite volume (r) is given by

$$(R_{\text{fluid}})_r = \frac{\mathrm{d}m_r}{\mathrm{d}t} - \sum_{\bar{e} \in r} \bar{\rho}_{w,er} \kappa_{er} (p_e - p_r) - q^{\text{in}}$$

$$= \frac{\mathrm{d}(\rho_r V_r)}{\mathrm{d}t} - \sum_{e \in r} \bar{\rho}_{er} \kappa_{er} (p_e - p_r) - q_r^{\text{in}}, \quad \text{where}$$

$$\kappa_{er} = \frac{a_r^3 l_e}{12\mu l_{er}}$$
(3)

with fluid pressure p_r on the face r, fluid pressure p_e on the edge e, the density of fluxed volume \bar{p}_{er} into the cell denoted with r from edge e and a source or sink term $q_r^{\rm in}$. Fluid pressure on the fracture surface and solid deformation are coupled to obtain fracture aperture and corresponding fracture storativity. An in-depth description of the framework can be found in Settgast et al. (2017).

Within this work, GEOS was extended to incorporate a locally variable mechanical and hydraulic aperture. Here the fracture aperture changes across the fracture plane, where each element used for flow along the fracture plane is assumed to consist of two parallel plates. This represents a local cubic law approach (Zimmerman & Yeo, 2000), which aims to account for hydraulic and mechanical effects introduced by rough fracture geometries, by assuming that smaller patches of the fracture can be approximated by a parallel plate model. Zimmerman and Yeo (2000) showed that the local cubic law provides a suitable approximation for fluid flow, but that it can lead to an overestimation of the local transmissivity, and that using Stokes equations will provide more accurate results. Factors which can weaken an approximation of fluid flow by the local cubic law can be roughness and flow tortuosity in the direction normal to the fracture and the neglecting of inertial forces (Wang et al., 2015). While mechanical and hydraulic apertures spatially vary, they are assumed to be equal for respective points in the fracture.

The advantage of this approach lies in the possibility to compute hydro-mechanical effects in the fracture plane, for rough fracture sets. While previous studies only simulate fluid flow in fractures (Wang et al., 2015; Zimmerman & Yeo, 2000) or do not model mechanical deformation during loading (Watanabe et al., 2008, 2009), the presented approach allows to estimate mechanical fracture deformation and the resulting fluid flow patterns and fluid pressure response in a fully coupled manner. Here it is noteworthy that the model only relies on the respective fracture geometry and a globally constant stiffness parameter accounting for material stiffness as model input. No further fitting, based on experimental results, is required or performed.

Within the scope of this study, we understand "fully coupled" hydro-mechanical processes to indicate mechanical stresses (or stress changes) closing the fracture and fluid pressures opening the fracture to be in equilibrium at all times. Changes in the mechanical loading or fluid injection rates influence each other so that stress changes yield a fluid pressure response and vice versa.

Since this study solves all equations in a fully coupled approach, especially very small fracture apertures can significantly increase the computational cost associated with the solving of the system of equations. For example, using a minimum hydraulic aperture of 0.1 μ m instead of 1 μ m to compute fluid flow would increase the range of the system of equations by 3 orders of magnitudes (due to flow being computed with the cubic law, equation (1)).

A minimum hydraulic aperture a_{\min} of 1 μ m and a maximum hydraulic aperture a_{\max} of 1 mm are therefore enforced in the numerical models to reduce nonlinearity of the system of equations which needs to be solved. The underlying assumption being, that values outside of this range do not alter the computed flow field and fluid pressure response. Sensitivity analysis showed the chosen minimum hydraulic fracture aperture to influence the results for values as low as 5 to 10 μm. Minimum hydraulic aperture values below 5 μm did not alter the pressure response significantly. Increasing the maximum hydraulic fracture aperture above 1 mm also did not alter the computed pressure response curves. Similar lower hydraulic aperture cutoffs were also proposed in studies focusing on solving fluid flow in rough fractures by Watanabe et al. (minimum hydraulic aperture of 1 μm) and Wang et al. (minimum hydraulic aperture of 10 μm) (Wang et al., 2015; Watanabe et al., 2008, 2009). While the presented method is not limited to the chosen minimum and maximum hydraulic aperture values, they simply represent the values chosen for this study to achieve faster numerical convergence.

Since this study solves the contact problem for locally varying mechanical apertures with a penalty method, the mechanical apertures need to become smaller than zero, to enforce a penalty and subsequently compute a local contact stress. Naturally, a hydraulic aperture below zero is not possible and a cutoff (here the minimum hydraulic aperture) has to be enforced, below which hydraulic and mechanical aperture cannot be equated. A constant fracture normal stiffness value is assumed across the fracture, which can be thought of as a globally applicable material constant. Locally, the penalty method uses a linear relation between fracture normal stiffness and the normal stress at the fracture surfaces. Globally, however, the spatially variable mechanical aperture can lead to a nonlinear fracture closure behavior, as will be demonstrated in this study. Nonlinear fracture closure with globally constant stiffness parameters can be obtained because the resistance of the fracture to a reduced aperture with higher loads increases as more area of the fracture comes into contact and the local penalty force is enforced or increases. While lower mechanical aperture values than zero are required to compute contact forces, values larger than zero do not alter the solution, since the fracture is then locally not in contact. Mechanical and hydraulic apertures are therefore only assumed to be equal for the range indicated above. For very low loads (e.g., 0.1 MPa), about 10 % of the total fracture area is at or near the upper aperture cutoff. This percentage decreases rapidly with increasing loads.

The specimen cylinders containing a fracture were simulated with increasing axial load σ_7 , with compressive stresses denoted as negative in the model. The aperture fields used for mechanics and fluid flow simulation in the fracture were obtained from matched surface scans of the fracture. Aperture fields were derived from the matched surface sides, by averaging the aperture (arithmetic average) over square areas with 0.1 mm edge length. On natural fractures, surface roughness variations can be expected for length scales ranging from µm to the long wavelength variations of fault zones. For the mesh size of the numerical model, we had to reach a compromise between rigorous physical coupling and ease of computation, as resolving fracture surface details down to the μm scale is generally not feasible. Since solving the contact problem of rough fractures fully coupled with fluid flow comes at considerable computational costs, we had to choose an element edge length that resolves large-scale (e.g., for the fracture surface in this study) roughness phenomena while still offering fast and stable computational results. For this purpose, we chose an element edge length below the grain sizes found in the specimens of this study (e.g., 3-8 mm). Specifically, the specimen is meshed with element edge lengths of about 2 mm throughout the domain. Aperture values on each node on the surface of the fracture are subsequently derived from the aperture field, which was computed from the fracture surface scans. Fluid flow and contact mechanics are solved on two adjacent element faces on the fracture surface and the element nodes, respectively. This means that the mechanical aperture is enforced at individual nodes, as the mechanical contact problem is solved by computing the penetration forces between two element nodes. The hydraulic aperture between two element faces is computed by averaging the mechanical apertures on the nodes surrounding each element face.

Experiment sets investigating mechanical closure behavior of heterogeneous fractures, contact stresses during loading and hydro-mechanical effects during loading were approached as follows.

- 1. Bulk mechanical behavior of the fracture. Mechanical closure behavior of the heterogeneous fractures was simulated dry. The aperture field measured before any testing was used as model input for the aperture distribution. Estimates of the joint normal stiffness are derived from average joint normal stiffness values obtained for increments of the fracture closure data measured during experiment Set I.
- 2. Hydro-mechanical effects during loading. The aperture field obtained after conclusion of all experiments is used for the HM-coupled simulations (Figure 2). Fracture aperture at the inlet in the center of the fracture is set to 1 mm to provide a sufficiently large aperture for fluid injection through the piping. As mentioned before, sensitivity analysis showed that larger maximum hydraulic apertures did not significantly alter the result but came at considerable computational cost. The constant injection rate used for the experiments (5 mL/min) is distributed evenly across the elements in the inlet. The boundary of the fracture is set to 1 mm aperture and atmospheric pressure conditions. Estimates of the joint normal stiffness are derived from average joint normal stiffness values obtained for increments of the fracture closure data measured during experiment Set ii.

3. Results

The aperture fields derived from matching both surface scans of the fractures before and after testing are shown in Figures 2a and 2c. Black regions are almost in contact, deep red regions signify small, and blue

21699356, 2018, 2, Downloaded from https://agupubs.onlinelibrary.wiley.com/doi/10.1002/2017JB015057, Wiley Online Library on [27/11/2025]. See the Terms and Conditions (https://onlinelibrary.wiley.com/com/erms-and-conditions) on Wiley Online Library for rules of use; OA articles are governed by the applicable Creative Commons License

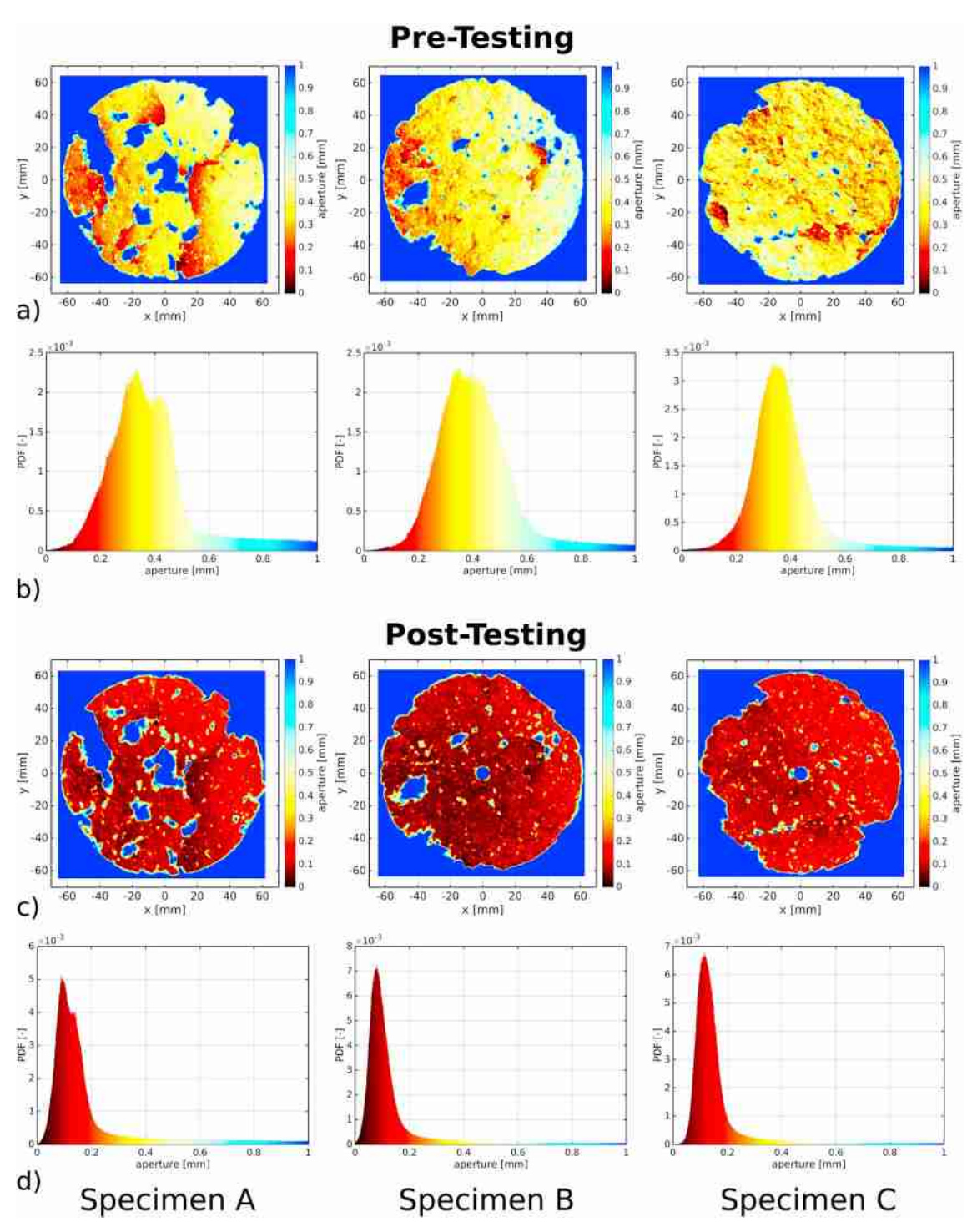


Figure 2. Aperture fields in the fracture as seen from above. Shown are Specimens A (left column), B (middle column), and C (right column). Aperture magnitude is given from 0 (black color) to 1 mm (blue color). (a) Aperture fields before testing; (b) histogram of aperture value distribution before testing; (c) aperture field after testing; and (d) histogram of aperture value distribution after testing.

21699356, 2018, 2, Downloaded from https://agupubs.onlinelibrary.wiley.com/doi/10.1002/2017JB015057, Wiley Online Library on [27/11/2025]. See the Terms and Conditions (https://onlinelibrary.wiley.com/terms

and-conditions) on Wiley Online Library for rules of use; OA articles are governed by the applicable Creative Commons License

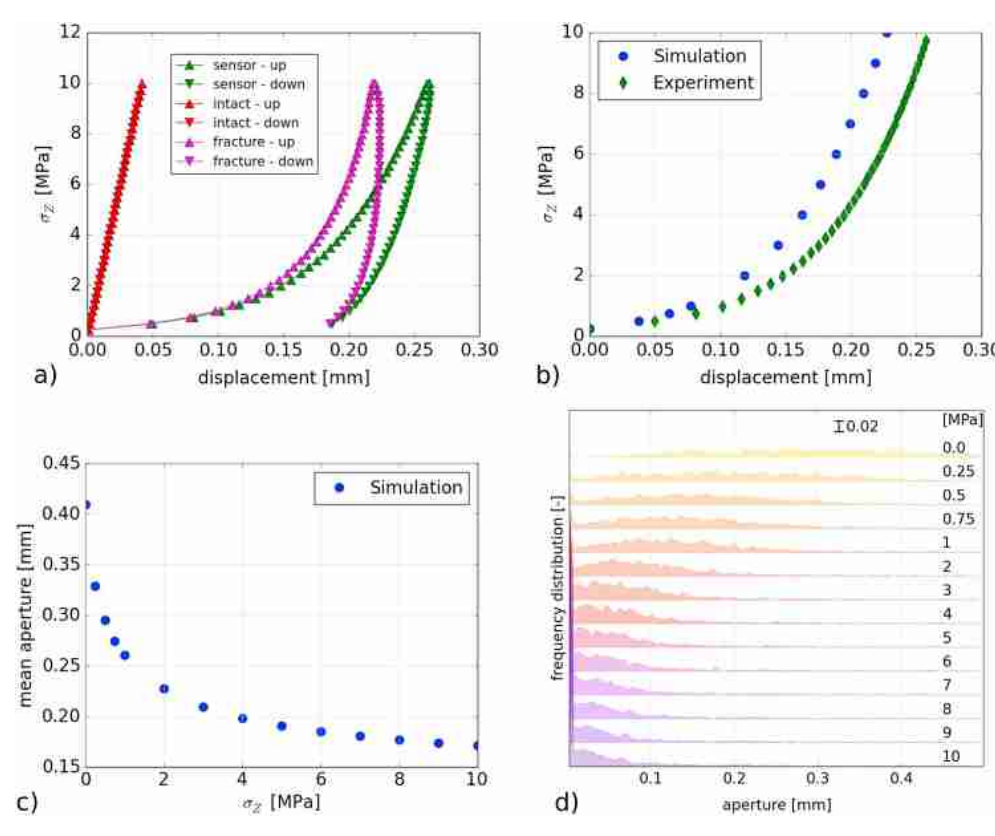


Figure 3. Experiment Set I—Specimen B. (a) Displacement between the sensor (green marker) is measured in the experiment. The theoretical elastic deformation of the intact rock mass (red marker) can be derived with the static Young's modulus. Fracture closure (magenta marker) consists of the difference between sensor measurements and elastic deformation. The deformation curves for increasing axial load are marked (\blacktriangle) and for decreasing axial load are marked (\blacktriangledown). (b) Mechanical displacement between sensor location as measured in the experiment (green marker) and numerical simulations (blue marker) is plotted versus axial load σ_Z . (c) Simulated mean aperture versus axial load σ_Z applied to the top of the cylinder. (d) Simulated histogram evolution of the aperture field over axial load σ_Z . The frequency distribution of aperture values is shifted with axial load σ_Z , to enable visual comparison of the shift of the histogram toward smaller aperture values with increasing σ_Z .

regions large apertures. Since most aperture regions are below 500 μ m and low aperture regions are most crucial for contact behavior, the maximum aperture displayed is 1 mm for all aperture fields for ease of comparison. The histogram of the aperture distribution is given below the respective aperture fields in Figures 2b and 2d.

3.1. Experiment Set I—Bulk Mechanical Behavior of the Fracture

The measured properties during experiment Set II was the mechanical deformation (displacement) of the specimens as recorded by the displacement transducer. The displacement transducer measures change in distance at two points on the specimen surface. Here two displacement transducers measure displacement on diagonally opposing sides of the specimen. If the base length between the two points is known, this displacement measurement can be expressed as strain. Representative behavior of fracture closure for specimen B is shown in Figure 3 for both experimental and numerical results. Figure 3a depicts experiment Set I with the respective sensor displacement (green), elastic deformation (red), and fracture displacement (magenta). Displacement per load increment is larger for lower stresses and starts to converge to a finite displacement for higher stress levels. Convergent fracture closure can be explained with increasing contact area in the fracture as load increases until the fracture aperture reaches a residual value and further increase in stress is taken up by the surrounding rock mass. For maximum axial load stresses of 10 MPa, a displacement of 0.26 mm is observed for specimen B (Specimen A; 0.16 mm, Specimen C; 0.34 mm). After reaching the maximum axial load stress of 10 MPa, the specimen is unloaded, during which irreversible displacement becomes apparent. After fully unloading the sample, irreversible displacements of 0.175 mm (Specimen B) were recorded (Specimen A; 0.055 mm, Specimen C; 0.24 mm). This is largely attributed to irreversible fracture closure,

frictional effects, and increased mating of the two fracture surfaces, since the intact rock mass is expected to behave predominantly elastic in this stress regime.

We compare the mechanical fracture closure results obtained from numerical simulations with the experimentally observed values in Figure 3b. Despite using a constant global normal stiffness estimated from experimental measurements, a nonlinear response for fracture closure is observed due to the heterogeneous character of the initial aperture field on the fracture surface. The mechanical displacement during specimen loading is modeled with a maximum error of about 12% (roughly 0.03 mm or 30 μ m) for large σ_Z (Figure 3b). The mean aperture decreases strongly for axial stress up to $\sigma_Z = 2$ MPa and then converges toward 0.17 mm mean aperture (Figure 3c). The aperture histogram evolution with increasing σ_Z characterizes the flow field response to fracture closure and is shown in Figure 3d. The aperture frequency distribution is fairly homogeneous between 0.1 and 0.5 mm for $\sigma_Z = 0$ MPa and starts rapidly compressing with increasing σ_Z . From 4 to 10 MPa, most aperture values are below 0.1 mm with only small further aperture decrease, as also observed in the mean aperture (Figure 3c).

The modeled stress distribution within the specimen and the increasing fracture closure with load are also displayed in Figure 4, which shows vertical stress distribution (σ_z) , the aperture field used as model input (for zero vertical load) and the aperture field for given load stages. Figure 4 shows the increasing stress concentrations around the fracture, where contact area leads to large vertical stresses while other regions near an open fracture show lower than average vertical stresses. The computed aperture field for a given applied load increasingly deviates from the original aperture field used as model input, even for vertical loads as small as 0.25 MPa. This shows the phenomena also observed in Figures 3b and 3c, where the largest changes of the fracture closure can be observed for early load stages where the fracture contacts offer the highest compliance. As can be seen in the top right parts of Figures 4a-4c, initial contact area is sparsely distributed across the fracture plane for low loads, but contact area increases with vertical load.

3.2. Experiment Set II — Hydro-Mechanical Effects

The measured properties during experiment Set II were the mechanical deformation (displacement) of the specimens as recorded by the displacement transducer and the fluid pressure necessary to sustain the given flow rates as measured at the pump. During increasing axial load σ_{Z} , fluid inlet pressures generally increased, the intact rock mass compressed, and the fracture closed.

Experimental data and numerical simulations are compared for the first load cycle of specimen B in Figures 5a and 5b. Displacement computed in a numerical simulation compares well to experimental data for σ_7 up to 2 MPa. For higher loads, the simulation behaves stiffer, with a maximum deviation from experimental data of 0.03 mm for σ_{Z} of 10 MPa. When comparing experiment Sets I and II, the maximum deviations of simulated and experimentally measured fracture closure are quite similar (around 0.03 mm). At low loads, the computed injection pressure is lower than measured data. For the whole load range, injection pressure predicts the experimentally observed trend while consistently underestimating the measured pressures by 0.2 to 0.5 MPa.

Simulation data for aperture, flow rate, and pressure distribution for axial loads of 0.25, 2, and 10 MPa are shown in Figures 6a – 6c. In Figure 6a, we plot the aperture distribution on the fracture predicted by the numerical simulation. To allow a comparison of all load stages, the color bar indicates apertures between 0 and 100 μ m. For low axial loads of $\sigma_Z = 0.25$ MPa, the aperture field is propped open by a few contact points (see Figure 6a), which significantly increase for $\sigma_7 = 2$ MPa (as seen in Figure 6b). Here larger connected regions close to or in contact emerge. At σ_7 of 10 MPa, the majority of the fracture aperture is below 30 μ m, with large aperture regions only sparsely connected. Specifically, roughly 10 % of the fracture area has aperture values below 10 μm and only 17% of the fracture has aperture values above 500 μm .

Fluid flow for low σ_Z in Figure 6a is distributed across the whole fracture, which could be expected, as the aperture in the fracture is larger than 50 µm except for a few contact points. As is apparent in the aperture field evolution (Figures 6a-6c), regions of contact or very small hydraulic aperture increase with loading, which leads to more pronounced flow channeling for σ_7 of 2 MPa (Figures 6b and 6c). At σ_7 of 10 MPa, two large and a few smaller flow channels emerge along regions of remaining high aperture, while large areas of the fracture do not experience significant flow.

Due to the small scale of the specimen, pressure diffusion causes an almost radially symmetric pressure field distribution across the fracture (Figures 6a-6c). Here the natural logarithm of the pressure is plotted with a maximum of 1.5 MPa to allow for comparison of pressures between all load stages. The pressure is largest

21699356, 2018, 2, Downloaded from https://agupubs.onlinelibrary.wiley.com/doi/10.10022017JB015057, Wiley Online Library on [27/1/12025]. See the Terms and Conditions (https://onlinelibrary.wiley.com/erms-and-conditions) on Wiley Online Library for rules of use; OA articles are governed by the applicable Cerative Commons License

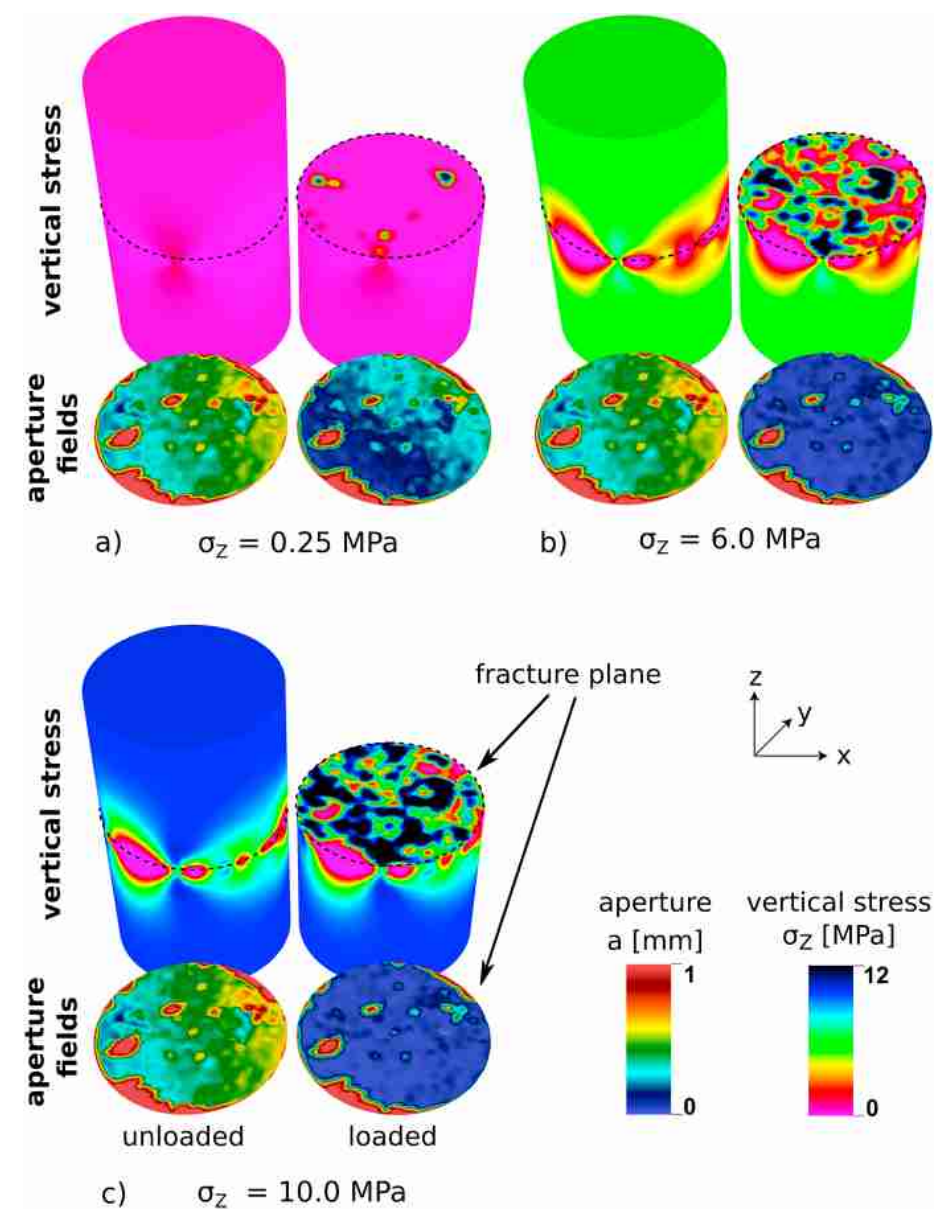


Figure 4. Experiment Set I — Specimen B. Top: Vertical stress σ_Z distribution in the whole specimen (left) and the lower half of the specimen, separated at the fracture (right). Bottom: Fracture aperture field for unloaded state (zero stress), used as model input (left) and fracture aperture field for given load stage (right). Shown are axial loading states for (a) $\sigma_Z=0.25$ MPa; (b) $\sigma_Z=6.0$ MPa; and (c) $\sigma_Z=10.0$ MPa. The specimen height is 225 mm, with a fracture plane diameter of 122 mm.

in the fracture center at the injection borehole and then rapidly declines over the first few centimeters, after which pressure gradients become significantly smaller. The pressure field is radial symmetric for low loads and starts to reflect preferential flow channels in the top left and bottom right for σ_7 of 10 MPa. Injection pressures show a stronger response for load changes near maximum $\sigma_{Z'}$ although the flow rate fields at 2 and 10 MPa are already in close resemblance.

4. Discussion

4.1. Experiment Set I — Mechanical Fracture Closure

The characteristic nonlinear shape of the displacement curve in this experiment (Figure 3) is captured by using the aperture field obtained from scanned surfaces during testing (Figure 2) and does not rely on numerical fitting. This means that neither the aperture field used as model input nor other physical parameters used to

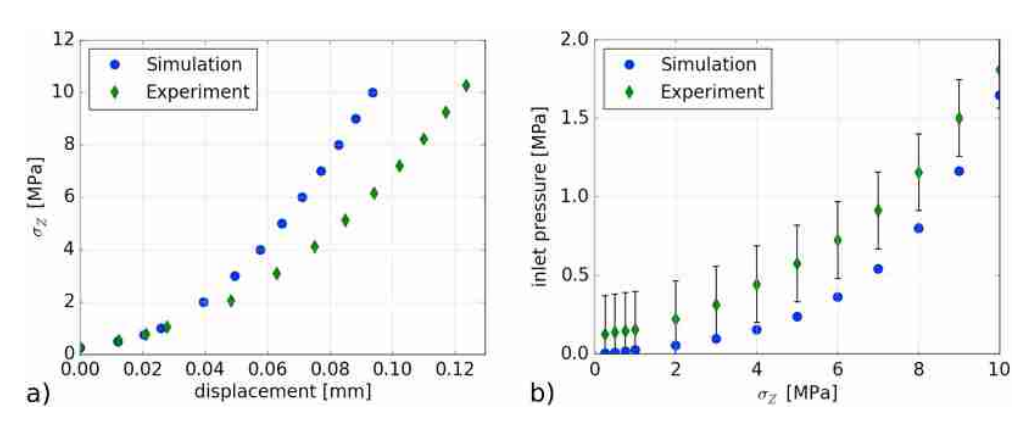


Figure 5. Experiment Set II — Specimen B. Comparison of experimental and simulation data for (a) σ_Z versus sensor displacement and (b) fluid pressure at the inlet versus σ_Z .

compute the hydro-mechanically coupled behavior of the specimen were adjusted to improve the accuracy of the results. The observed convergent displacement with increasing axial load is also reported in the literature for other experiments on fractures (Bandis et al., 1983; Barton et al., 1985; Zangerl et al., 2008). This nonlinear fracture closure during loading is linked to the increase in contact area (Figure 4), as the two rock surfaces experience more resistance against compression with increasing contact area.

For this experiment series, artificial tensile fractures with pronounced surface roughness and highly variable aperture fields were used. Fractures with less surface roughness (e.g., saw cut fractures) would be expected to display a much less pronounced nonlinearity in their closure behavior (see also Figure 3).

Despite preloading the fractures, discrepancies between experimental and numerical results could be caused by shear displacement, frictional effects during shearing, rotation, plastic deformation, seating, and mating of the fractures in the experiments. The errors associated with the applied load and displacement measurement are too small to explain any deviations of experimental and simulated data, as they are smaller than the plotted marker size. The nonlinear decrease of aperture, shown in Figure 3c, goes in line with the fracture closure shown in Figures 3a and 3b, as mean aperture is expected to decrease with fracture closure. While aperture data without axial load can be obtained from surface scans (Figure 2), capturing aperture fields under compression requires extensive laboratory equipment, such as CT scans, which are often tied to specific resolutions or limitations regarding the mechanical or hydraulic boundary conditions which can be applied. Instead, numerical simulations which capture the mechanical fracture behavior can be employed, to gain insights into aperture behavior during compression (Figures 3c and 3d). Here a nonlinear fracture closure behavior also yields a nonlinear mean aperture decrease (Figure 3c).

4.2. Experiment Set II — Hydro-Mechanical Effects

Analogous to loading the fracture without fluid injection, fracture closure is dominated by the applied σ_Z . Despite fluid injection pressures increasing up to 6 MPa in the most extreme test, fluid pressure diffusion in the model causes a rapid pressure decline over just 1 to 2 cm on the laboratory scale (Figure 6), which causes fracture closure to remain relatively unaffected by high-fluid injection pressures. Nonlinear fracture closure leads to only small fracture opening at high σ_Z if the effective normal stress is lowered by fluid injection pressures (Figure 6). This further pronounces the small effect of fluid injection pressures on fracture opening. The significantly reduced total fracture closure for experiment Set II (Figure 6) is related to the corresponding fracture aperture field which was determined after testing concluded (Figure 2).

The hydro-mechanically coupled model captures the characteristic behavior of both fracture closure and fluid injection pressure increase. Fluid flow behavior is dominated by the fracture aperture field and its response to increasing axial load. This demonstrates the value for numerical frameworks capturing the mechanical behavior of rough fractures and flow, as fluid flow is strongly dependent on the smallest aperture values which define flow channels and act as a bottleneck (Figure 6). The strong influence of the smallest aperture regions on fluid flow was also pointed out by Tsang (Tsang, 1984). HM-coupled numerical frameworks simulating phenomena in rough fractures cannot only be employed to simulate processes on the laboratory scale, for specific specimen, but also to derive averaged behavior and constitutive laws on the field scale, which can be derived from fracture data on smaller scale.

21699356, 2018, 2, Downloaded from https://agupubs.onlinelibrary.wiley.com/doi/10.1002/2017JB015057, Wiley Online Library on [27/11/2025]. See the Terms and Conditions (https://onlinelibrary.wiley.com/terms-and-conditions) on Wiley Online Library for rules of use; OA articles are governed by the applicable Ceatwice Commons License

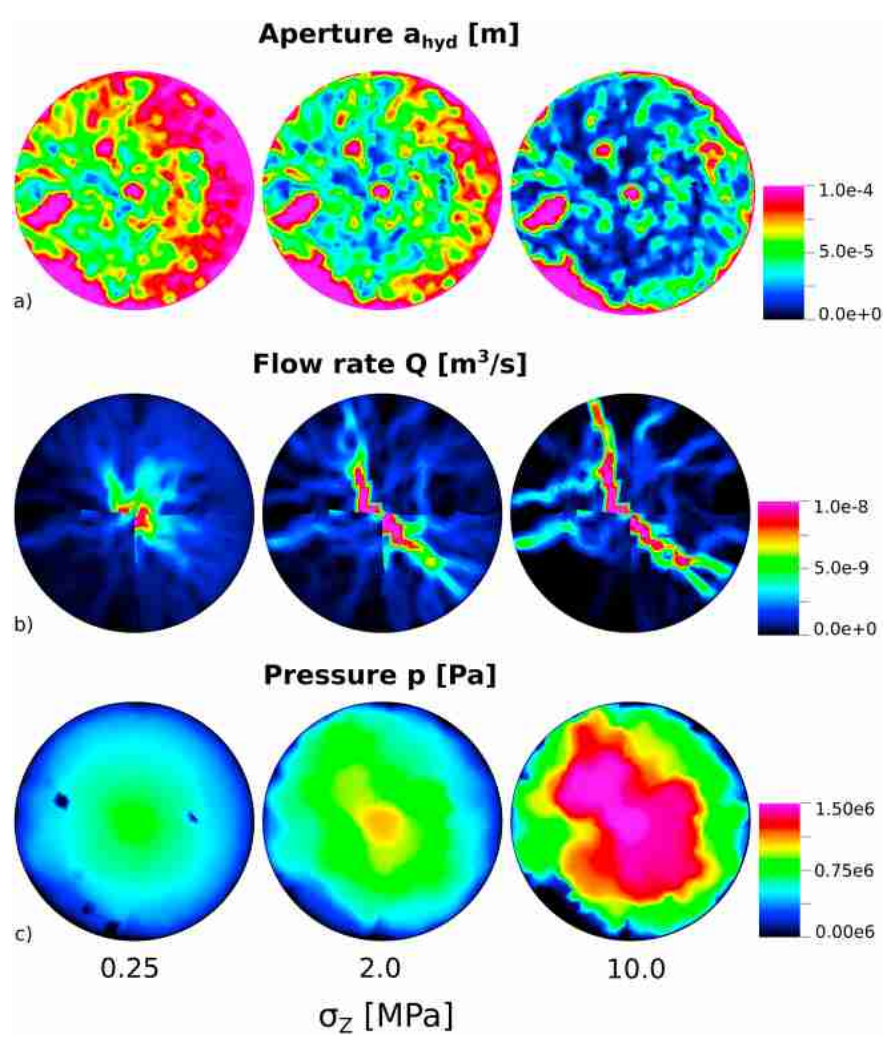


Figure 6. Simulation of experiment Set II — Specimen B of aperture (top row), flow rate (middle row) and pressure (bottom row) for 0.25 (left column); 2 (center column) and 10 MPa (right column). Discontinuities in the flow rate magnitude can be observed along segmentation boundaries for the parallelization, which is a visualization artifact on segmentation boundaries associated with the flow rate magnitude estimation on nodes from flow rates computed across element edges.

It is noteworthy that none of the modeled aperture fields in this particular study resulted in flow rates dominated by large aperture regions. However, this could depend on the aperture field configuration, as fracture surfaces and fracture aperture fields are highly unique (Vogler, Amann, et al., 2016; Vogler, Walsh, Bayer, & Amann, 2017). This study used artificial fractures obtained from tensile tests, where some areas of the fracture surfaces experienced breakouts during splitting of the core. As this material was removed for the laboratory experiments, the presented aperture fields might lead to different flow characteristics than the aperture field of a natural fracture.

Injection pressures were underestimated for low loads by the numerical model, which could be caused by (1) using locally averaged aperture values (local cubic law) or (2) small shear movements and rotations of the experiment specimen, which are not captured in the simulations. Usage of the local cubic law could result in locally averaged aperture values which offer little resistance to fluid flow as the fracture is mainly open for low σ_7 . In the experiment, flow could encounter a small aperture bottleneck of a few μm in flow path length, which might not be captured due to the element edge length constraints of the mesh employed in the simulations. Matedness of the fracture could also change by shear movements and rotation of the fracture specimens, which could result in a different aperture field than the one used as simulation input. Discrepancies in experimental and simulated injection pressures can also be partially attributed to measurement errors.



AGU Journal of Geophysical Research: Solid Earth

10.1002/2017JB015057

However, experimental measurements show a smooth response to the fracture deformation (Figure 5), and no oscillations or other measurement fluctuations could be observed. Given the smooth fluid pressure response, and since fluid flow into the fracture cannot be induced with negative pump pressures, the error associated with injection pressures is most likely significantly lower than the maximum error associated with maximum injection pressures of the pump (at around 50 MPa). Nonetheless, mechanical and hydro-mechanical effects during axial loading of the specimen were captured in the numerical model while using the aperture field under zero stress state as model input and not performing numerical fitting.

It should be noted that the presented experiments were performed on granodiorite specimens, which have a low permeability, and do not display a pronounced poroelastic effect for the applied fluid pressures. However, other rock types such as carbonates or clays may display a stronger poroelastic response during fluid pressurization, such as pressure solution or swelling (Fang et al., 2017; Yasuhara et al., 2004).

5. Conclusions

The presented study utilizes a fully hydro-mechanically coupled model to further the understanding of coupled processes of fluid flow in heterogeneous fractures. Results demonstrate that fracture closure behavior and corresponding fluid pressure response observed in laboratory experiments can be captured with a local cubic law model with spatially variable mechanical and hydraulic aperture.

Based on aperture field input, the model computes aperture field changes, contact areas, stress distributions within the specimen, and changes of fluid flow distributions with increasing vertical loading. For loading of a dry specimen, the model captures the nonlinear fracture closure increase with loading which is observed in experiments of this work and previous studies. During fluid injection under fracture compression, the numerical framework reproduces the nonlinear fracture behaviors with maximum deviations of 10% for fracture closure and 0.2 to 0.5 MPa for the fluid injection pressure response.

Through these experimental and numerical investigations, the possibility of scaling fracture roughness effects for both mechanical and hydraulic properties is possible in the future. While this work compared experiments and simulations in a single fracture, further investigations are needed to study the hydro-mechanical interactions between multiple rough fractures.

Notation

```
a aperture (m);
a_{\text{hyd}} hydraulic aperture (m);
a_{\text{max}} maximum hydraulic aperture (m);
a_{\text{mech}} mechanical aperture (m);
a_{\min} minimum hydraulic aperture (m);
   b_i body force (gravity) (m<sup>2</sup>/s);
    i spatial direction (–):
    k contact stiffness (Pa/m);
    n face normal vector (–):
    p fluid pressure (Pa);
   p_e fluid pressure at edge e (Pa);
   p_r fluid pressure on face r (Pa);
  p<sub>ini</sub> fluid injection pressure (Pa);
   \Phi finite element shape function (–);
  q_r^{\rm in} source or sink term (m<sup>3</sup>/s);
   Q flow rate (m^3/s);
   \hat{Q} normalized flow rate (–);
    t_i externally applied traction (Pa);
   T_{ii} Cauchy stress tensor (Pa);
    u displacement across the fracture surface (m);
    x jump in displacement across the fracture (m);
    \Gamma external boundary of solid body (–);
```

 μ dynamic viscosity of water (Pa s);

21699356, 2018, 2, Downloaded from https://agupubs.onlinelibrary.wiley.com/doi/10.10022017JB015057, Wiley Online Library on [27/1/12025]. See the Terms and Conditions (https://onlinelibrary.wiley.com/erms-and-conditions) on Wiley Online Library for rules of use; OA articles are governed by the applicable Cerative Commons License

 Ω solid body (–);

 ρ_m solid body density (kg/m³);

 ρ_w fluid density (kg³/m³);

 $\bar{\rho}_{er}$ fluxed volume into the cell r from edge e (m³/s);

 σ_Z stress in the z direction (Pa).

Acknowledgments References

The authors want to thank the chair of geosensors and engineering geodesy at ETH Zurich and especially Robert Presl for their support with the photogrammetry scanner. The authors gratefully acknowledge R. Seifert for assistance with laboratory equipment. This work was partially supported by the GEOTHERM II project, which is funded by the Competence Center Environment and Sustainability of the ETH Domain. We would like to thank the Editor André Revil and Associate Editor Ludmila Adam for handling the manuscript and the reviewer Mark McClure and an anonymous reviewer for their time and valuable feedback. Data employed in this study can be found in the presented figures and by contacting the corresponding author Daniel Vogler at davogler@ethz.ch.

- Annavarapu, C., Settgast, R. R., Johnson, S. M., Fu, P., & Herbold, E. B. (2015). A weighted Nitsche stabilized method for small-sliding contact on frictional surfaces. Computer Methods in Applied Mechanics and Engineering, 283, 763-781, https://doi.org/10.1016/i.cma.2014.09.030
- Bandis, S., Lumsden, A., & Barton, N. (1983). Fundamentals of rock joint deformation. International Journal of Rock Mechanics and Mining Sciences and Geomechanics Abstracts, 20(6), 249-268.
- Barton, N., Bandis, S., & Bakhtar, K. (1985). Strength, deformation and conductivity coupling of rock joints. International Journal of Rock Mechanics and Mining Sciences, 22(3), 121-140.
- Brown, S. R. (1987). Fluid flow through rock joints: The effect of surface roughness. Journal of Geophysical Research, 92(B2), 1337 1347. Cappa, F., & Rutqvist, J. (2011). Modeling of coupled deformation and permeability evolution during fault reactivation induced by deep underground injection of CO₂. International Journal of Greenhouse Gas Control, 5(2), 336-346. https://doi.org/10.1016/j.jiggc.2010.08.005
- Chen, Z., Narayan, S., Yang, Z., & Rahman, S. (2000). An experimental investigation of hydraulic behaviour of fractures and joints in granitic rock. International Journal of Rock Mechanics and Mining Sciences, 37(7), 1061 – 1071.
- Cook, N. G. W. (1992). Natural joints in rock—Mechanical, hydraulic and seismic behavior and properties under normal stress. International Journal of Rock Mechanics and Minina Sciences and Geomechanics Abstracts, 29(3), 198-223.
- Derode, B., Cappa, F., Guglielmi, Y., & Rutqvist, J. (2013). Coupled seismo-hydromechanical monitoring of inelastic effects on injection-induced fracture permeability. International Journal of Rock Mechanics and Mining Sciences, 61, 266-274. https://doi.org/10.1016/i.iirmms.2013.03.008
- Esaki, T., Du, S., Mitani, Y., Ikusada, K., & Jing, L. (1999). Development of a shear-flow test apparatus and determination of coupled properties for a single rock joint. International Journal of Rock Mechanics and Mining Sciences, 36(5), 641-650.
- Fang, Y., Elsworth, D., Wang, C., Ishibashi, T., & Fitts, J. P. (2017). Frictional stability-permeability relationships for fractures in shales. Journal of Geophysical Research: Solid Earth, 122, 1760-1776. https://doi.org/10. 1002/2016JB013435
- Figueiredo, B., Tsang, C.-F., Rutqvist, J., Bensabat, J., & Niemi, A. (2015). Coupled hydro-mechanical processes and fault reactivation induced by CO₂ injection in a three-layer storage formation. International Journal of Greenhouse Gas Control, 39, 432-448. https://doi.org/10.1016/j.ijggc.2015.06.008
- Figueiredo, B., Tsang, C.-F., Rutqvist, J., & Niemi, A. (2015). A study of changes in deep fractured rock permeability due to coupled hydro-mechanical effects. International Journal of Rock Mechanics and Mining Sciences, 79, 70-85. https://doi.org/10.1016/j.ijrmms.2015.08.011
- Fu, P., Cruz, L., Moos, D., Settgast, R. R., & Ryerson, F. J. (2015). Numerical investigation of a hydraulic fracture bypassing a natural fracture in 3D. San Francisco, CA: American Rock Mechanics Association.
- Fu, P., Hao, Y., Walsh, S. D. C., & Carrigan, C. R. (2016). Thermal drawdown-induced flow channeling in fractured geothermal reservoirs. Rock Mechanics and Rock Engineering, 49(3), 1001 – 1024. https://doi.org/10.1007/s00603-015-0776-0
- GOM mbH (2017). GOM: Atos core. Retrieved from http://www.atos-core. com/en/industries.php
- Gu, S., Liu, Y., & Chen, Z. (2014). Numerical study of dynamic fracture aperture during production of pressure-sensitive reservoirs. International Journal of Rock Mechanics and Mining Sciences, 70, 229-239.
- Guo, B., Fu, P., Hao, Y., Peters, C. A., & Carrigan, C. R. (2016). Thermal drawdown-induced flow channeling in a single fracture in EGS. Geothermics, 61, 46-62.
- Hakami, E., & Larsson, E. (1996). Aperture measurements and flow experiments on a single natural fracture. International Journal of Rock Mechanics and Mining Sciences and Geomechanics Abstracts, 33(4), 395-404.
- Lee, H. S., & Cho, T. F. (2002). Hydraulic characteristics of rough fractures in linear flow under normal and shear load. Rock Mechanics and Rock Engineering, 35(4), 299-318. https://doi.org/10.1007/s00603-002-0028-y
- Li, B., Jiang, Y., Koyama, T., Jing, L., & Tanabashi, Y. (2008). Experimental study of the hydro-mechanical behavior of rock joints using a parallel-plate model containing contact areas and artificial fractures. International Journal of Rock Mechanics and Mining Sciences, 45(3),
- Louis, C. (1969). A study of groundwater flow in jointed rock and its influence on the stability of rock masses (10 ed.). (Rock Mechanics Research Report). London: Imperial College of Science and Technology.
- McClure, M. W., & Horne, R. N. (2014a). An investigation of stimulation mechanisms in enhanced geothermal systems. International Journal of Rock Mechanics and Mining Sciences, 72(0), 242 – 260. https://doi.org/10.1016/j.ijrmms.2014.07. 011
- McClure, M. W., & Horne, R. N. (2014b). Correlations between formation properties and induced seismicity during high pressure injection into granitic rock. Engineering Geology, 175(0), 74-80. https://doi.org/10.1016/j.engqeo.2014.03.015
- Min, K., Lee, J., & Stephansson, O. (2013). Implications of thermally-induced fracture slip and permeability change on the long-term performance of a deep geological repository. International Journal of Rock Mechanics and Mining Sciences, 61, 275-288. https://doi.org/10.1016/i.iirmms.2013.03.009
- Nemoto, K., Watanabe, N., Hirano, N., & Tsuchiya, N. (2009). Direct measurement of contact area and stress dependence of anisotropic flow through rock fracture with heterogeneous aperture distribution. Earth and Planetary Science Letters, 281(1-2), 81-87. https://doi.org/10.1016/j.epsl.2009.02.005
- Oron, A. P., & Berkowitz, B. (1998). Flow in rock fractures: The local cubic law assumption reexamined. Water Resources Research, 34(11), 2811-2825. https://doi.org/10.1029/98WR02285
- Park, H., Osada, M., Matsushita, T., Takahashi, M., & Ito, K. (2013). Development of coupled shear-flow-visualization apparatus and data analysis. International Journal of Rock Mechanics and Mining Sciences, 63, 72–81. https://doi.org/10.1016/j.ijrmms.2013.06.003
- Pyrak-Nolte, L. J., & Morris, J. P. (2000). Single fractures under normal stress: The relation between fracture specific stiffness and fluid flow. International Journal of Rock Mechanics and Mining Sciences, 37(1-2), 245-262. https://doi.org/10.1016/s1365-1609(99)00104-5
- Raven, K. G., & Gale, J. E. (1985). Water-flow in a natural rock fracture as a function of stress and sample-size. International Journal of Rock Mechanics and Minina Sciences, 22(4), 251-261.
- Renshaw, C. E. (1995). On the relationship between mechanical and hydraulic apertures in rough-walled fractures. Journal of Geophysical Research, 100(B12), 24,629-24,636. https://doi.org/10.1029/95JB02159

- Rutqvist, J., & Stephansson, O. (2003). The role of hydromechanical coupling in fractured rock engineering. Hydrogeology Journal, 11(1),
- Settgast, R. R., Johnson, S. M., Fu, P., & Walsh, S. D. (2014). Simulation of hydraulic fracture networks in three dimensions utilizing massively parallel computing resources. In Unconventional Resources Technology Conference (pp. 1730 – 1737). Denver, CO: URTEC-1923299-MS. https://doi.org/10.15530/urtec-2014-1923299
- Settgast, R. R., Johnson, S. M., Fu, P., Walsh, S. D., & Ryerson, F. J. (2012). Simulation of hydraulic fracture networks in three dimensions. In Stanford Geothermal Workshop (pp. 1-5). Palo Alto: Stanford University Press.
- Settgast, R. R., Fu, P., Walsh, S. D., White, J. A., Annavarapu, C., & Ryerson, F. J. (2017). A fully coupled method for massively parallel simulation of hydraulically driven fractures in 3-dimensions. International Journal for Numerical and Analytical Methods in Geomechanics, 41, 627-653. https://doi.org/10.1002/nag.2557
- Tsang, Y. W. (1984). The effect of tortuosity on fluid-flow through a single fracture. Water Resources Research, 20(9), 1209 1215. https://doi.org/10.1029/WR020i009p01209
- Vogler, D. (2016). Hydro-mechanically coupled processes in heterogeneous fractures: Experiments and numerical simulations (PhD thesis), ETH Zurich, Zurich, Switzerland,
- Vogler, D., Amann, F., Bayer, P., & Elsworth, D. (2016). Permeability evolution in natural fractures subject to cyclic loading and gouge formation. Rock Mechanics and Rock Engineering, 49(9), 3463-3479. https://doi.org/10.1007/s00603-016-1022-0
- Vogler, D., Settgast, R. R., Annavarapu, C., Bayer, P., & Amann, F. (2016). Hydro-mechanically coupled flow through heterogeneous fractures. In Proceedings of the 41st Workshop on Geothermal Reservoir Engineering. Palo Alto: Stanford University Press, SGP-TR-209.
- Vogler, D., Settgast, R. R., Gischig, V. S., Jalali, M., Doetsch, J., Valley, B., ... Amann, F. (2017). Modeling the hydraulic fracture stimulation performed for reservoir permeability enhancement at the Grimsel Test Site, Switzerland. In Proceedings of the 42nd Workshop on Geothermal Reservoir Engineering (pp. 1–9). Palo Alto: Stanford University Press.
- Vogler, D., Walsh, S. D. C., Bayer, P., & Amann, F. (2017). Comparison of surface properties in natural and artificially generated fractures in a crystalline rock. Rock Mechanics and Rock Engineering, 50(11), 2891 - 2909. https://doi.org/10.1007/s00603-017-1281-4
- Vogler, D., Walsh, S. D. C., Dombrovski, E., & Perras, M. A. (2017). A comparison of tensile failure in 3D-printed and natural sandstone. Engineering Geology, 226, 221-235. https://doi.org/10.1016/j.enggeo.2017.06.011
- Walsh, J. B. (2003). A theoretical analysis of sliding of rough surfaces. Journal of Geophysical Research, 108(B8), 2385. https://doi.org/10.1029/2002JB002127
- Walsh, S. D. C., & Carroll, S. A. (2013). Fracture-scale model of immiscible fluid flow. Physical Review E, 87(1), 013012. https://doi.org/10.1103/PhysRevE.87.013012
- Walsh, S. D. C., Frane, W. L. Du, Mason, H. E., & Carroll, S. A. (2013). Permeability of wellbore-cement fractures following degradation by carbonated brine. Rock Mechanics and Rock Engineering, 46(3), 455-464. https://doi.org/10.1007/s00603-012-0336-9
- Walsh, S. D. C., Du Frane, W. L., Sholokhova, Y., Settgast, R. R., Johnson, S. M., & Carroll, S. A. (2012). Chemo-mechanical permeability evolution In wellbore-cement fractures exposed to carbon-dioxide-rich brines. In 46th US Rock Mechanics/Geomechanics Symposium (pp. 1-7). American Rock Mechanics Association.
- Wang, L., Cardenas, M. B., Slottke, D. T., Ketcham, R. A., & Sharp, J. M. (2015). Modification of the local cubic law of fracture flow for weak inertia, tortuosity, and roughness. Water Resources Research, 51(4), 2064-2080. https://doi.org/10.1002/2014WR015815
- Watanabe, N., Hirano, N., & Tsuchiya, N. (2008). Determination of aperture structure and fluid flow in a rock fracture by high-resolution numerical modeling on the basis of a flow-through experiment under confining pressure. Water Resources Research, 44(6), W06412. https://doi.org/10.1029/2006WR005411
- Watanabe, N., Hirano, N., & Tsuchiya, N. (2009). Diversity of channeling flow in heterogeneous aperture distribution inferred from integrated experimental-numerical analysis on flow through shear fracture in granite. Journal of Geophysical Research, 114, B04208. https://doi.org/10.1029/2008 JB005959
- Witherspoon, P. A., Wang, J. S. Y., Iwai, K., & Gale, J. E. (1980). Validity of cubic law for fluid-flow in a deformable rock fracture. Water Resources Research, 16(6), 1016-1024.
- Xiong, X., Li, B., Jiang, Y., Koyama, T., & Zhang, C. (2011). Experimental and numerical study of the geometrical and hydraulic characteristics of a single rock fracture during shear. International Journal of Rock Mechanics and Mining Sciences, 48(8), 1292 – 1302.
- Yasuhara, H., Elsworth, D., & Polak, A. (2004), Evolution of permeability in a natural fracture; Significant role of pressure solution, Journal of Geophysical Research, 109, B03204. https://doi.org/10.1029/2003JB002663
- Yeo, I. W., De Freitas, M. H., & Zimmerman, R. W. (1998). Effect of shear displacement on the aperture and permeability of a rock fracture. International Journal of Rock Mechanics and Mining Sciences, 35(8), 1051-1070.
- Zangerl, C., Evans, K. F., Eberhardt, E., & Loew, S. (2008). Normal stiffness of fractures in granitic rock: A compilation of laboratory and in-situ experiments. International Journal of Rock Mechanics and Mining Sciences, 45(8), 1500 – 1507.
- Zimmerman, R. W., & Bodvarsson, G. S. (1996). Hydraulic conductivity of rock fractures. Transport in Porous Media, 23(1), 1-30.
- Zimmerman, R. W., Kumar, S., & Bodvarsson, G. S. (1991). Lubrication theory analysis of the permeability of rough-walled fractures. International Journal of Rock Mechanics and Mining Sciences and Geomechanics Abstracts, 28(4), 325-331.
- Zimmerman, R. W., & Yeo, I. W. (2000). Fluid flow in rock fractures: From the Navier-Stokes equations to the cubic law. In B. Faybishenko, S. Benson, & P. Witherspoon (Eds.), Dynamics of fluids in fractured rock (pp. 213 – 224). Washington, DC: American Geophysical Union.
- Zou, L., Jing, L., & Cvetkovic, V. (2015). Roughness decomposition and nonlinear fluid flow in a single rock fracture. International Journal of Rock Mechanics and Mining Sciences, 75, 102-118. https://doi.org/10.1016/j.ijrmms.2015.01.016